Thermodynamic Effects Are Essential for Surface Entrapment of Bacteria

Premkumar Leishangthem[1] and Xinliang Xu[1,2,*]
[1]Complex Systems Division, Beijing Computational Science Research Center, Beijing 100193, China
[2]Department of Physics, Beijing Normal University, Beijing 100875, China

(Received 27 July 2023; revised 12 March 2024; accepted 17 April 2024; published 3 June 2024)

The entrapment of bacteria near boundary surfaces is of biological and practical importance, yet the underlying physics is not well understood. We demonstrate that it is crucial to include a commonly neglected thermodynamic effect related to the spatial variation of hydrodynamic interactions, through a model that provides analytic explanation of bacterial entrapment in two dimensionless parameters: α_1 the ratio of thermal energy to self-propulsion, and α_2 an intrinsic shape factor. For α_1 and α_2 that match an *Escherichia coli* at room temperature, our model quantitatively reproduces existing experimental observations, including two key features that have not been previously resolved: The bacterial "nose-down" configuration, and the anticorrelation between the pitch angle and the wobbling angle. Furthermore, our model analytically predicts the existence of an entrapment zone in the parameter space defined by $\{\alpha_1, \alpha_2\}$.

DOI: 10.1103/PhysRevLett.132.238302

Swimming microorganisms are constantly influenced by the presence of boundary surfaces in their natural habitat, giving rise to rich swimming behaviors [1,2]. One phenomenon commonly known as surface entrapment attracts particular interest, where the swimmer moves along near the surface for a prolonged time [3]. Since its first discovery in bull spermatozoa [4], such entrapment is widely observed for a variety of microorganisms in both the domain Bacteria (e.g., *Escherichia coli* [5]) and the domain Eukaryota (e.g., *Tetrahymena pyriformis* [6]) in different types of fluids [7], and around surfaces with different properties [8]. In addition to its importance to many biological processes such as fertilization [9,10] and biofilm formation [11], such surface-swimmer interaction also provides insight for the design of microfluidic structures [12] and artificial microswimmers [13–15] for desired transport properties. However, the underlying mechanism is still poorly understood.

Using *E. coli* as an example where experimental data are abundant, we provide a theoretic study explaining the dynamics of flagellar bacteria near surfaces. In the early time when bacterial accumulation near a plane was experimentally observed [16], it is under debate if hydrodynamic interactions are essential [17,18], as the observed surface accumulation can also be explained by stochastic models without hydrodynamic interactions [19]. Dynamical behaviors of trapped bacteria are then systematically studied [3,5,7,20–22]. While it is shown that stochastic effects such as rotational noise [23] or bacterial tumbling [24] are significantly suppressed during the entrapment [25,26], a recent experiment suggested that the near-field hydrodynamic interaction plays the major role [27]. However, two features among the many observations, i.e., the "nose-down" configuration and the anticorrelation between the pitch angle and the wobbling angle [5], become distinguished due to their challenges to all existing theories. Specifically, numerical simulations with full hydrodynamic interactions for no-slip plane show a "nose-up" configuration [28–30], and suggest a positive correlation between the wobbling angle and the pitch angle [31]. We shall demonstrate that a commonly neglected thermodynamic effect is essential. When this crucial effect is incorporated, even a simplified model of the hydrodynamic interactions can quantitatively explain the two key features, as well as other observed surface entrapment behaviors.

Problem formulation for nonwobbling bacteria.—For simplicity, we first study a nonwobbling bacterial model which allows an analytic solution. Swimming in a fluid of viscosity μ above an infinitely large plane with no-slip boundary at $x = 0$, an *E. coli* bacterium is simplified as two spheres, a body sphere with radius R_b and a tail sphere with radius R_t, connected by a rigid rod that separates the two centers by l [inset in Fig. 1(a)] [32]. The tail sphere is

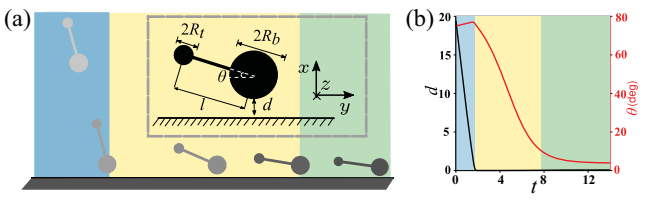

FIG. 1. (a) For a bacterium modeled as two spheres connected by a rod (inset), its trajectory demonstrates surface entrapment. (b) The temporal evolutions of d (black line) and θ (red line) show a three-stage dynamics visualized by blue, yellow, and green shaded areas, respectively.

propelled by a phantom force $\boldsymbol{F}_{\rm act}$ provided by the spinning of flagella that is not treated explicitly. Each configuration is fully determined by the surface distance d between bacterial body and the plane, and pitch angle θ which is positive for a "nose-down" configuration.

Since the characteristic size and speed are about 1 μm and 10 μm/sec, respectively, in water the corresponding Reynolds number is low (10^{-5}) so that bacterial flows are typically studied by the linear Stokes equation. At a time resolution $\Delta t \approx 10^{-2}$ sec the system is in the overdamped limit described by

$$\boldsymbol{\xi} \cdot \mathbf{U} = \mathbf{F}^{\rm P} + \mathbf{F}^{\rm B}, \tag{1}$$

where the resistance tensor $\boldsymbol{\xi}$ for any configuration is fully determined by hydrodynamics, $\mathbf{U} \equiv (\boldsymbol{u}_{\rm b}, \boldsymbol{\omega}_{\rm b}, \boldsymbol{u}_{\rm t}, \boldsymbol{\omega}_{\rm t})^T$ is the translational/rotational velocity vector with indice "b" ("t") standing for body sphere (tail sphere), $\mathbf{F}^{\rm P} \equiv (\boldsymbol{F}_{\rm b}, \boldsymbol{L}_{\rm b}, \boldsymbol{F}_{\rm t}, \boldsymbol{L}_{\rm t})^T$ represents the nonhydrodynamic forces, and $\mathbf{F}^{\rm B}$ represents stochastic forces.

At absolute-zero temperature, $\mathbf{F}^{\rm B} = 0$. Eq. (1) reduces to

$$\begin{pmatrix} \boldsymbol{F}_{\rm b} \\ \boldsymbol{L}_{\rm b} \\ \boldsymbol{F}_{\rm t} \\ \boldsymbol{L}_{\rm t} \end{pmatrix} = \begin{pmatrix} \xi^{\rm FU}_{\rm bb} & \xi^{\rm F\omega}_{\rm bb} & \xi^{\rm FU}_{\rm bt} & \xi^{\rm F\omega}_{\rm bt} \\ \xi^{\rm LU}_{\rm bb} & \xi^{\rm L\omega}_{\rm bb} & \xi^{\rm LU}_{\rm bt} & \xi^{\rm L\omega}_{\rm bt} \\ \xi^{\rm FU}_{\rm tb} & \xi^{\rm F\omega}_{\rm tb} & \xi^{\rm FU}_{\rm tt} & \xi^{\rm F\omega}_{\rm tt} \\ \xi^{\rm LU}_{\rm tb} & \xi^{\rm L\omega}_{\rm tb} & \xi^{\rm LU}_{\rm tt} & \xi^{\rm L\omega}_{\rm tt} \end{pmatrix} \cdot \begin{pmatrix} \boldsymbol{u}_{\rm b} \\ \boldsymbol{\omega}_{\rm b} \\ \boldsymbol{u}_{\rm t} - \boldsymbol{u}_0 \\ \boldsymbol{\omega}_{\rm t} \end{pmatrix}, \tag{2}$$

where $\boldsymbol{u}_0 \equiv (\xi^{\rm FU}_{\rm tt})^{-1} \cdot \boldsymbol{F}_{\rm act}$. The system is fully determined with two widely used conditions: (i) the free-swimming condition, i.e., $\boldsymbol{F}_{\rm b} = -\boldsymbol{F}_{\rm t} \equiv \boldsymbol{F}_{\rm eff}$ and $\boldsymbol{L}_{\rm b} = -\boldsymbol{L}_{\rm t} - (\boldsymbol{r}_{\rm t} - \boldsymbol{r}_{\rm b}) \times \boldsymbol{F}_{\rm t} \equiv -\boldsymbol{L}_{\rm eff} + \boldsymbol{F}_{\rm eff} \times (\boldsymbol{r}_{\rm b} - \boldsymbol{r}_{\rm t})$ and (ii) the rigid body condition, i.e., $\boldsymbol{\omega}_{\rm b} = \boldsymbol{\omega}_{\rm t} \equiv \boldsymbol{\omega}_0$ and $\boldsymbol{u}_{\rm t} = \boldsymbol{u}_{\rm b} + \boldsymbol{\omega}_0 \times (\boldsymbol{r}_{\rm t} - \boldsymbol{r}_{\rm b})$. Equation (2) is then solved for $\boldsymbol{F}_{\rm eff}$, $\boldsymbol{L}_{\rm eff}$, $\boldsymbol{\omega}_0$, and $\boldsymbol{u}_{\rm b}$, leading to system evolution $\Delta \mathbf{R} = \mathbf{U} \Delta t$.

At finite temperature, $\mathbf{F}^{\rm B} \neq 0$. By integrating Eq. (1) over Δt, a timescale much larger than the Brownian timescale $\tau_{\rm B} \sim 10^{-6}$ sec yet still small that changes in configurations are insignificant, we get two additional terms in system evolution [33–35]:

$$\Delta \mathbf{R} = \mathbf{U} \Delta t + k_{\rm B} T \boldsymbol{\nabla} \cdot \boldsymbol{\xi}^{-1} \Delta t + \mathbf{X}(\Delta t), \tag{3}$$

where $\mathbf{X}(\Delta t)$ is a random displacement characterized by $\langle \mathbf{X}(\Delta t) \rangle = 0$ and $\langle \mathbf{X}(\Delta t) \mathbf{X}(\Delta t) \rangle = 2 k_{\rm B} T \boldsymbol{\xi}^{-1} \Delta t$.

For an entrapped *E. coli*, we have $d/R_{\rm b} \sim 0.1$ so small that terms in $\boldsymbol{\xi}$ become large, in agreement with experimental observation of suppressed $\mathbf{X}(\Delta t)$ [25] that we choose to treat as negligible during entrapment. On the other hand, while commonly neglected in previous numerical studies [28,29,31], the thermodynamic term $k_{\rm B} T \boldsymbol{\nabla} \cdot \boldsymbol{\xi}^{-1}$ describes the spatial variations in diffusivity, and in the $d \to 0$ limit remains a finite constant independent of d. Therefore, the evolution equation becomes $\Delta \mathbf{R} = \mathbf{U}' \Delta t$ with $\mathbf{U}' \equiv (\boldsymbol{u}'_{\rm b}, \boldsymbol{\omega}'_{\rm b}, \boldsymbol{u}'_{\rm t}, \boldsymbol{\omega}'_{\rm t})^T = \mathbf{U} + k_{\rm B} T \boldsymbol{\nabla} \cdot \boldsymbol{\xi}^{-1}$, where $\mathbf{U}$ satisfies Eq. (2) and the rigid body condition changes to $\boldsymbol{\omega}'_{\rm b} = \boldsymbol{\omega}'_{\rm t} \equiv \boldsymbol{\omega}_0$ and $\boldsymbol{u}'_{\rm t} = \boldsymbol{u}'_{\rm b} + \boldsymbol{\omega}_0 \times (\boldsymbol{r}_{\rm t} - \boldsymbol{r}_{\rm b})$.

Numerical simulation.—For a typical *E. coli* in water at room temperature, we estimate that $k_{\rm B} T \approx 4 \times 10^{-21}$ Nm, $\mu \approx 10^{-3}$ N sec/m^2, $|\boldsymbol{F}_{\rm act}| \approx 4 \times 10^{-13}$ N, $R_{\rm b} \approx 1$ μm, $l \approx 5$ μm, and $R_{\rm t} \approx 0.4$ μm [36–38]. Using 1 μm and 1 sec as the unit of length and time respectively and setting $\mu = 1$ for the unit of force, such a bacterium is characterized by $\{l = 5, R_{\rm b} = 1, R_{\rm t} = 0.4, |\boldsymbol{F}_{\rm act}| = 400, k_{\rm B} T = 4\}$. In Fig. 1(a) we show its dynamics moving toward the plane, simulated assuming only hydrodynamic interactions without steric interactions. The key in this simulation is getting $\boldsymbol{\xi}$ for each configuration, which is constructed following the Stokesian dynamics simulation [35,39] in a two-step procedure. Specifically, we first obtain the far-field mobility tensor through $\boldsymbol{M}_\infty = \boldsymbol{M}_0 + \hat{\boldsymbol{M}}$. Here $\boldsymbol{M}_0$ is the analytic far-field hydrodynamic interaction without plane [40], and the plane contribution $\hat{\boldsymbol{M}}$ is analytically available through the method of images [39]. In the second step, $\boldsymbol{\xi}$ is obtained through $\boldsymbol{\xi} = \boldsymbol{M}_\infty^{-1} + \boldsymbol{\xi}_{\rm b}$, with $\boldsymbol{\xi}_{\rm b}$ the lubrication between body sphere and the plane [41,42].

As illustrated by the temporal evolution of d and θ in Fig. 1(b), our numerical results reproduce the experimentally observed three-stage dynamics [5]: the initial approach where d drops quickly with an almost constant θ; the reorientation stage where $\tan\theta$ decays exponentially right after d becomes smaller than $R_{\rm b}$ (Fig. S1 in the Supplemental Material [43]); and the steady swimming stage where both $\dot{d}$ and $\dot{\theta}$ gradually decay to zero characterizing a stable entrapment. Such dynamics can also be illustrated in the phase diagram defined by d and θ [Fig. 2(a)], where steady swimming corresponds to a stable fixed point with $\theta > 0$ (a "nose-down" configuration), in agreement with experimental observations.

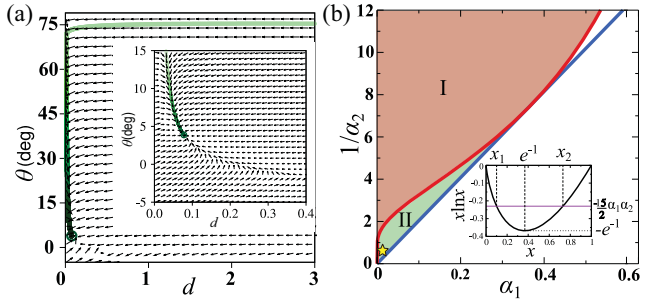

FIG. 2. (a) In the phase diagram defined by d and θ, bacterial trajectory (green line) approaches to a stable fixed point (green circle). (b) The parameter space defined by α_1 and α_2 can be divided into three regions: region I (red) above the red line $\alpha_2 = -(2/15)\ln\alpha_1$, region II (green) between the red line and blue line $(15/2)\alpha_1\alpha_2 = e^{-1}$ with $\alpha_1 \leq e^{-1}$, and the region outside. A typical *E. coli* at room temperature (yellow star) is in region II. The inset in (b) shows $x \ln x$ versus x.

Analytic solution.—To understand these results, we simplify the problem with two ideal approximations. Since $l \gg R_t$, our first approximation assumes that the tails are not hydrodynamically coupled with the body or the plane so that body-tail coupling $\boldsymbol{\xi}_{bt} = \boldsymbol{\xi}_{tb} = 0$, and tail self-term $\boldsymbol{\xi}_{tt}$ is a constant. Therefore, the only configurational dependent term in $\boldsymbol{\xi}$ is $\boldsymbol{\xi}_{bb}$, which is an analytical function of single parameter d/R_b in the $d \to 0$ limit [40]. Since d/R_b is small during entrapment, our second approximation uses this analytical $\boldsymbol{\xi}_{bb}$ function for all d of interest. These two approximations lead to a simplified $k_B T \boldsymbol{\nabla} \cdot \boldsymbol{\xi}^{-1}$ with only one nonzero component: A constant velocity $\boldsymbol{v} = (k_B T/6\pi\mu R_b^2)\hat{\boldsymbol{x}}$ for bacterial body moving away from the plane (see the Supplemental Material, Sec. A [43]).

To obtain fixed points in the phase diagram defined by d and θ, we insert $\dot{d} = \dot{\theta} = 0$ into Eq. (2), which gives

$$(\boldsymbol{\xi}_{bb}^{LU})_{zy}(\boldsymbol{u}_b' \cdot \hat{\boldsymbol{y}}) = (\boldsymbol{\xi}_{tt}^{FU})_{yy}(\boldsymbol{u}_b' \cdot \hat{\boldsymbol{y}}) l \sin\theta \tag{4}$$

$$|\boldsymbol{F}_{act}| \sin\theta = (\boldsymbol{\xi}_{bb}^{FU})_{xx}(\boldsymbol{v} \cdot \hat{\boldsymbol{x}}) \tag{5}$$

Here Eq. (4) is equivalent to the fifth equation in [27], which characterizes the torque balance on the body sphere in $\hat{\boldsymbol{z}}$, between the boundary-induced torque due to bacterial body translation $\boldsymbol{u}_b' \cdot \hat{\boldsymbol{y}}$ along the plane (lhs) and the torque arising from the friction against bacterial tail translation (rhs). Equation (5) characterizes the force balance on the body sphere in $\hat{\boldsymbol{x}}$, between self-propulsion (lhs) and the thermodynamic effect we introduced (rhs). The coefficients are available from lubrication theory as $(\boldsymbol{\xi}_{bb}^{LU})_{zy} = -6\pi\mu R_b^2 (2/15)\ln(d/R_b)$, $(\boldsymbol{\xi}_{tt}^{FU})_{yy} = 6\pi\mu R_t$, $(\boldsymbol{\xi}_{bb}^{FU})_{xx} = 6\pi\mu R_b^2/d$.

For $\boldsymbol{u}_b' \cdot \hat{\boldsymbol{y}} \neq 0$, Eqs. (4) and (5) can be further reduced in terms of two dimensionless parameters $\alpha_1 \equiv k_B T/|\boldsymbol{F}_{act}|R_b$ and $\alpha_2 \equiv R_t l/R_b^2$:

$$\frac{d}{R_b}\ln\frac{d}{R_b} = -\frac{15\alpha_1\alpha_2}{2} \tag{6}$$

$$\ln\frac{d}{R_b} = -\frac{15\alpha_2 \sin\theta}{2} \tag{7}$$

with prefactor $15/2$ arising from translation-rotation coupling $(\boldsymbol{\xi}_{bb}^{LU})_{zy}$.

Dictated by Eqs. (6) and (7), two curves become important in the parameter space defined by α_1 and α_2. The first curve, $(15/2)\alpha_1\alpha_2 = e^{-1}$ [blue line in Fig. 2(b)], arises from the fact that $(d/R_b)\ln(d/R_b) \geq -e^{-1}$ for $d > 0$ where equality happens at $d/R_b = e^{-1}$ [Fig. 2(b) inset]. Thus, fixed points ($\{d_1, \theta_1\}$ and $\{d_2, \theta_2\}$) only exist when $0 \geq -(15/2)\alpha_1\alpha_2 \geq -e^{-1}$, with $0 \leq d_1/R_b \leq e^{-1} \leq d_2/R_b \leq 1$. The second curve, $\alpha_2 = -(2/15)\ln\alpha_1$ [red line in Fig. 2(b)], is obtained by assuming $\sin\theta = 1$, the largest possible value for $\sin\theta$. Our analysis shows that (See Sec. C in the Supplemental Material), for parameter choice $\{\alpha_1, \alpha_2\}$ above the red line in Fig. 2(b) (region I), only a saddle point $\{d_2, \theta_2\}$ with $d_2/R_b > e^{-1}$ exists. For parameter choice $\{\alpha_1, \alpha_2\}$ between the red line and blue line with $\alpha_1 \leq e^{-1}$ in Fig. 2(b) (region II), both fixed points exist, where $\{d_1, \theta_1\}$ with $d_1/R_b < e^{-1}$ is always stable, while $\{d_2, \theta_2\}$ with $d_2/R_b > e^{-1}$ is always a saddle point. No fixed point exists for $\{\alpha_1, \alpha_2\}$ outside region I and II. Since physically observed entrapment is associated only with a stable fixed point, region II defines the entrapment zone: No entrapment can be observed for $\{\alpha_1, \alpha_2\}$ outside the zone.

For a typical *E. coli* at room temperature, we have $\{l = 5, R_b = 1, R_t = 0.4, |\boldsymbol{F}_{act}| = 400, k_B T = 4\}$, leading to $\{\alpha_1 = 0.01, \alpha_2 = 2\}$ that falls in the entrapment zone [Fig. 2(b)]. For this set of $\{\alpha_1, \alpha_2\}$, we predict the stable fixed point at $d^* = 0.05$ μm from Eq. (6) and then $\theta^* = 12°$ from Eq. (7). This is within the experimentally observed range for d between 0.03 μm and 0.25 μm [21], and in agreement with the observation of θ with a mean of 10° [5]. Furthermore, our simulations for bacteria with various shapes ($0.3 \leq R_t \leq 0.5$, $5 \leq l \leq 9$) are in good agreement with Eqs. (6) and (7) as illustrated by Fig. S5(a) and Fig. S5(b) in the Supplemental Material. In contrast, with $\alpha_1 = 0$ (neglecting the thermodynamic effect), a bacterium of any shape falls in region I [Fig. 2(b)], where only a "nose-up" saddle point exists that is irrelevant to the experimentally observed bacterial entrapment (Sec. E in the Supplemental Material [43]).

Bacterial wobbling.—For the nonwobbling bacterial model above, the body-tail connection is treated as rigid without considering the self-spinning of either the bacterial body or the flagellar bundle, i.e., $\boldsymbol{\omega}_b = \boldsymbol{\omega}_t = \boldsymbol{\omega}_0$. In the real world, the self-spinning of the two parts, $\boldsymbol{\omega}_b^0$ and $\boldsymbol{\omega}_t^0$, respectively, are generally not collinear [Fig. 3(a)]. For free-swimming bacteria the nonzero angle γ formed by the two vectors leads to a center of mass rotation $\boldsymbol{\omega}_0$ generally not aligned with its translation and therefore, bacterial wobbling. To account for the wobbling, we generalize the nonwobbling bacterial model by explicit consideration of $\boldsymbol{\omega}_b^0$ and $\boldsymbol{\omega}_t^0$, and replace the rigid connection by a universal joint through relation $R_b^3|\boldsymbol{\omega}_b^0|\cos\gamma = R_t^3|\boldsymbol{\omega}_t^0|$ [38,44] where $|\boldsymbol{\omega}_t^0| = 100$ Hz fixed to match the experiments [36] (Supplemental Material [43], Sec. D). The overall rotations for bacterial body and flagellar bundle are $\boldsymbol{\omega}_b = \boldsymbol{\omega}_b^0 + \boldsymbol{\omega}_0$ and $\boldsymbol{\omega}_t = \boldsymbol{\omega}_t^0 + \boldsymbol{\omega}_0$, respectively.

With this generalization, we numerically study the dynamics of wobbling bacteria near a plane, where each configuration is now determined by d and two distinct pitch angles, θ_b and θ_t [Fig. 3(a)]. For illustration purposes, in Fig. 3 we highlight the self-spinning by drawing an ellipsoid and a helix in place of the body sphere and tail sphere used in our actual simulations. Our results show that bacteria can be trapped in clockwise circular trajectories when viewed from above [Fig. 3(b)]. For a typical bacterium ($l = 5$, $R_b = 1$, $R_t = 0.4$) with $\gamma = 30°$ at room

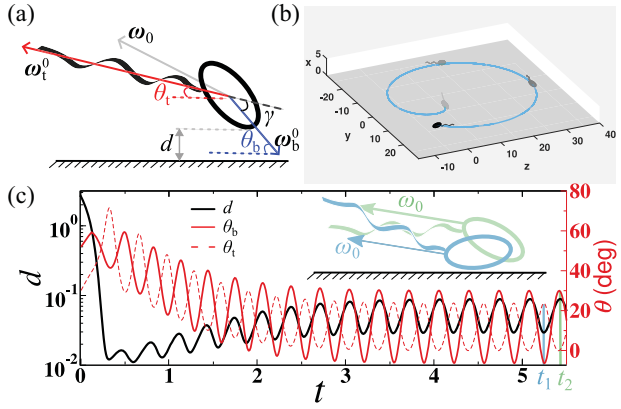

FIG. 3. (a) Our model of a wobbling bacterium. (b) Bacterial trajectory near a plane. (c) The temporal evolutions of d (solid black), θ_b (solid red), and θ_t (dash red). Blue (green) bar indicates time t_1 (t_2) when θ_b is smallest (largest) during entrapment, with the corresponding configurations shown in the inset using actual θ_b and θ_t, and exaggerated d.

temperature, in Fig. 3(c) we show the temporal evolution of d, θ_b, and θ_t. During the entrapment stage, all these three variables are periodically oscillating with the same frequency, where d and θ_b are almost in phase while θ_t has nearly an opposite phase [Fig. 3(c)]. In the inset, we show the bacterial configurations at t_1 (t_2) with smallest (largest) θ_b denoted as $\theta_{\min}$ ($\theta_{\max}$). The experimentally recorded average pitch angle $\bar{\theta}$ and wobbling angle θ_w [5] can be obtained through $\bar{\theta} \equiv (\theta_{\max} + \theta_{\min})/2$ and $\theta_w \equiv (\theta_{\max} - \theta_{\min})/2$. Similarly, we define $\bar{d} \equiv (d_{\max} + d_{\min})/2$.

A variety of bacteria characterized by $\{l, R_b, R_t, \gamma\}$ are then simulated at room temperature, where for γ we sampled 20°, 30°, and 40°, and for each of the other three parameters we limit the variations to at most 20% from the corresponding value of a typical *E. coli*. The scatter plot of all $\{\bar{\theta}, \theta_w\}$ obtained from the entrapment stage show an anticorrelation spreading broadly along the $\bar{\theta} = \theta_w$ direction [Fig. 4(a)], in quantitative agreement with previous experiment (Fig. 4 in [5]).

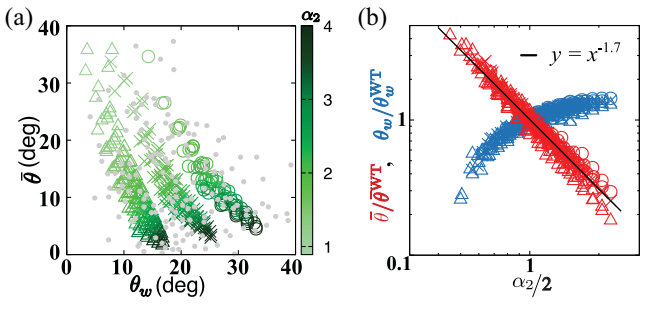

FIG. 4. Simulation data with $\gamma = 20°$ (triangles), $\gamma = 30°$ (crosses), and $\gamma = 40°$ (circles) yield the scatter plot $\{\bar{\theta}, \theta_w\}$ (green) in (a), normalized $\bar{\theta}$ (red) and θ_w (blue) as functions of α_2 in (b). Results from [5] are shown as gray dots in (a).

Interesting results emerge when sorting out our data by γ. For each specific γ we observe an anticorrelation with a much narrower spread, which is regulated by α_2 in a quantitatively similar fashion. Specifically, for each γ we plot $\bar{\theta}$ (θ_w) as a function of α_2, normalized by $\bar{\theta}^{WT}$ (θ_w^{WT}) obtained from a typical bacterium with that particular γ. Our data from three distinct γ collapse, indicating the existence of two master curves for $\bar{\theta}/\bar{\theta}^{WT}$ and θ_w/θ_w^{WT} respectively [Fig. 4(b)].

The results above can be explained by Eqs. (6) and (7), which are still valid for wobbling bacteria if we replace $\{d, \theta\}$ in the equations by $\{\bar{d}, \bar{\theta}\}$ observed in the data (Fig. S5 in the Supplemental Material [43]). Since we are in the parameter range in which changes in $\ln(\bar{d}/R_b)$ are less significant than changes in $\bar{d}/R_b$, for an estimate we neglect changes in $\ln(\bar{d}/R_b)$, which leads to $\bar{d}/R_b \sim \alpha_1\alpha_2$ according to Eq. (6) and $\sin\bar{\theta} \approx \bar{\theta} \sim \alpha_2^{-1}$ according to Eq. (7). This estimate correctly captures the positive (negative) correlation between $\bar{d}/R_b$ ($\bar{\theta}$) and α_2, in qualitative agreement with numerical fit of our data that $\bar{d}/R_b \sim \alpha_2^{1.8}$ [Fig. S6(a)], $\ln(\bar{d}/R_b) \sim \alpha_2^{-0.6}$ [Fig. S6(b)], and $\bar{\theta} \sim \alpha_2^{-1.7}$ [Fig. 4(b)]. As it is experimentally established that wobbling can be significantly suppressed by nearby boundaries [38,45], the positive correlation between $\bar{d}/R_b$ and α_2 leads to a positive correlation between θ_w and α_2, and thus the anticorrelation between $\bar{\theta}$ and θ_w.

Beyond the "nose-down" configuration and the anticorrelation between $\bar{\theta}$ and θ_w, our numerical results are also in quantitative agreement with other experimental observations (Sec. D2 in the Supplemental Material [43]), including the clockwise direction of circular trajectories [7,16]; the range of the observed radii of the circles (denoted as R_c) [7,20], and the range of $\bar{d}$ [21]; positive correlations between R_c and d [21], R_c and α_1 [22], and R_c and α_2 [3]; and an anticorrelation between $\bar{\theta}$ and $\bar{d}$ [3].

Discussion.—In this study we ignore stochastic effects $\mathbf{X}(\Delta t)$ and bacterial tumbling. At a cost of making trapped bacteria incapable of escaping, this simplification helps us identify entrapment as a fixed point and highlight the importance of the thermodynamic effect $k_B T \nabla \cdot \boldsymbol{\xi}^{-1}$. An estimate of $\mathbf{X}(\Delta t)$ near the fixed point shows that it only becomes important at timescales much larger than the entrapment process (Sec. F in the Supplemental Material [43]), and eventually leads to bacterial escape that is out of the scope of the current work.

For the entrapment stage, the self-propulsion for the "nose-down" configuration needs to be balanced by a cell-plane repulsion. At room temperature and $d \approx 0.1$ μm, a thermodynamic repulsion arises naturally, and explains all existing observations with even a simplified model that considers the bacterial body (flagellar bundle) as a sphere with the size equal to its hydrodynamic radius. For future experiments to verify if other mechanisms such as steric interactions also contribute, our model provides the following

predictions: (i) The entrapped configuration $\{d, \theta\}$ is dictated by $\alpha_1 \equiv k_B T/|\boldsymbol{F}_{act}|R_b$ and $\alpha_2 \equiv R_t l/R_b^2$, through Eqs. (6) and (7). Extra care is needed for studies at different temperatures, as self-propulsion can triple with a slight increase of $k_B T$ from 20 °C to 40 °C [22]. (ii) About the flagellar bundle, the orientation θ_t has an opposite phase with respect to d and θ_b; and the variation in γ is the main factor underlying the broad spread of $\{\bar{\theta}, \theta_w\}$ data along the $\bar{\theta} = \theta_w$ direction. (iii) There exists an entrapment zone within the range of $0 < \alpha_1 < e^{-1}$ and $\alpha_2 > 2/15$.

Three implications follow from (iii). First, entrapment is a special feature for active systems, and no entrapment is allowed for passive systems (zero activity and thus $\alpha_1 = \infty$) at any temperature. Second, entrapment is not available for swimmers with $\alpha_2 \equiv R_t l/R_b^2 < 2/15$, which provides a guideline for controlling biological and engineering active swimmers near surfaces. Third, while entrapment only exists at low temperatures that satisfy $\alpha_1 \equiv k_B T/|\boldsymbol{F}_{act}|R_b < e^{-1}$, at the lowest temperature, i.e., the absolute zero, the stable fixed point no longer exists: according to Eq. (6), d needs to be zero, which is singular that no θ can satisfy Eq. (7). This explains why negligence of $k_B T \boldsymbol{\nabla} \cdot \boldsymbol{\xi}^{-1}$ in previous studies, which is equivalent to setting the temperature to zero, cannot reproduce the entrapment correctly. Instead, a finite temperature is essential for achieving the physical entrapment.

We thank X. Cheng, L. S. Luo, M. Stynes, Y. L. Wu, J. H. Yuan, and H. P. Zhang for helpful discussions. This work is supported by NSFC No. 11974038 and No. U2230402. We also acknowledge the computational support from the Beijing Computational Science Research Center.

*xinliang@csrc.ac.cn

[1] V. Kantsler, J. Dunkel, M. Polin, and R. E. Goldstein, Proc. Natl. Acad. Sci. U.S.A. **110**, 1187 (2013).
[2] M. Contino, E. Lushi, I. Tuval, V. Kantsler, and M. Polin, Phys. Rev. Lett. **115**, 258102 (2015).
[3] R. Di Leonardo, D. Dell'Arciprete, L. Angelani, and V. Iebba, Phys. Rev. Lett. **106**, 038101 (2011).
[4] Rothschild, Nature (London) **198**, 1221 (1963).
[5] S. Bianchi, F. Saglimbeni, and R. Di Leonardo, Phys. Rev. X **7**, 011010 (2017).
[6] T. Ohmura, Y. Nishigami, A. Taniguchi, S. Nonaka, J. Manabe, T. Ishikawa, and M. Ichikawa, Proc. Natl. Acad. Sci. U.S.A. **115**, 3231 (2018).
[7] D. Cao, M. Dvoriashyna, S. Liu, E. Lauga, and Y. L. Wu, Proc. Natl. Acad. Sci. U.S.A. **119**, e2212078119 (2022).
[8] A. Poddar, A. Bandopadhyay, and S. Chakraborty, J. Fluid Mech. **894**, A11 (2020).
[9] C. K. Tung and S. S. Suarez, Cells **10**, 1297 (2021).
[10] M. R. Raveshi, M. S. A. Halim, S. N. Agnihotri, M. K. O'Bryan, A. Neild, and R. Nosrati, Nat. Commun. **12**, 3446 (2021).
[11] C. D. Nadell, K. Drescher, and K. R. Foster, Nat. Rev. Microbiol. **14**, 589 (2016).
[12] A. Dehkharghani, N. Waisbord, J. Dunkel, and J. S. Guasto, Proc. Natl. Acad. Sci. U.S.A. **116**, 11119 (2019).
[13] J. Simmchen, J. Katuri, W. E. Uspal, M. N. Popescu, M. Tasinkevych, and S. Sánchez, Nat. Commun. **7**, 10598 (2016).
[14] C. Liu, C. Zhou, W. Wang, and H. P. Zhang, Phys. Rev. Lett. **117**, 198001 (2016).
[15] S. Ketzetzi, J. de Graaf, R. P. Doherty, and D. J. Kraft, Phys. Rev. Lett. **124**, 048002 (2020).
[16] P. D. Frymier, R. M. Ford, H. C. Berg, and P. T. Cummings, Proc. Natl. Acad. Sci. U.S.A. **92**, 6195 (1995).
[17] A. P. Berke, L. Turner, H. C. Berg, and E. Lauga, Phys. Rev. Lett. **101**, 038102 (2008).
[18] S. E. Spagnolie and E. Lauga, J. Fluid Mech. **700**, 105 (2012).
[19] G. Li and J. X. Tang, Phys. Rev. Lett. **103**, 078101 (2009).
[20] E. Lauga, W. R. DiLuzio, G. M. Whitesides, and H. A. Stone, Biophys. J. **90**, 400 (2006).
[21] G. L. Li, L. K. Tam, and J. X. Tang, Proc. Natl. Acad. Sci. U.S.A. **105**, 18335 (2008).
[22] K. Maeda, Y. Imae, J. I. Shioi, and F. Oosawa, J. Bacteriol. **127**, 1039 (1976).
[23] K. Schaar, A. Zöttl, and H. Stark, Phys. Rev. Lett. **115**, 038101 (2015).
[24] G. Junot, T. Darnige, A. Lindner, V. A. Martinez, J. Arlt, A. Dawson, W. C. K. Poon, H. Auradou, and E. Clément, Phys. Rev. Lett. **128**, 248101 (2022).
[25] K. Drescher, J. Dunkel, L. H. Cisneros, S. Ganguly, and R. E. Goldstein, Proc. Natl. Acad. Sci. U.S.A. **108**, 10940 (2011).
[26] M. Molaei, M. Berry, R. Stocker, and J. Sheng, Phys. Rev. Lett. **113**, 068103 (2014).
[27] O. Sipos, K. Nagy, R. Di Leonardo, and P. Galajda, Phys. Rev. Lett. **114**, 258104 (2015).
[28] D. Giacché, T. Ishikawa, and T. Yamaguchi, Phys. Rev. E **82**, 056309 (2010).
[29] D. Pimponi, M. Chinappi, P. Gualtieri, and C. M. Casciola, J. Fluid Mech. **789**, 514 (2016).
[30] S. E. Spagnolie, G. R. Moreno-Flores, D. Bartolo, and E. Lauga, Soft Matter **11**, 3396 (2015).
[31] T. Eisenstecken, H. Hu, and R. G. Winkler, Soft Matter **12**, 8316 (2016).
[32] B. K. Zhang, P. Leishangthem, Y. Ding, and X. L. Xu, Proc. Natl. Acad. Sci. U.S.A. **118**, e2100145118 (2021).
[33] D. L. Ermak and J. A. McCammon, J. Chem. Phys. **69**, 1352 (1978).
[34] P. S. Grassia, E. J. Hinch, and L. C. Nitsche, J. Fluid Mech. **282**, 373 (1995).
[35] J. F. Brady and G. Bossis, Annu. Rev. Fluid Mech. **20**, 111 (1988).
[36] N. C. Darnton, L. Turner, S. Rojevsky, and H. C. Berg, J. Bacteriol. **189**, 1756 (2007).
[37] M. Dvoriashyna and E. Lauga, PLoS One **16**, e0254551 (2021).
[38] S. Kamdar, S. Shin, P. Leishangthem, L. F. Francis, X. L. Xu, and X. Cheng, Nature (London) **603**, 819 (2022).

[39] J. W. Swan and J. F. Brady, Phys. Fluids **19**, 113306 (2007).
[40] D. J. Jeffrey and Y. Onishi, J. Fluid Mech. **139**, 261 (1984).
[41] G. Bossis, A. Meunier, and J. D. Sherwood, Phys. Fluids A **3**, 1853 (1991).
[42] A. J. Goldman, R. G. Cox, and H. Brenner, Chem. Eng. Sci. **22**, 637 (1967).
[43] See Supplemental Material at http://link.aps.org/supplemental/10.1103/PhysRevLett.132.238302 for more details about theoretical derivation, simulation data, and the effect of random noises.
[44] Y. Shimogonya, Y. Sawano, H. Wakebe, Y. Inoue, A. Ishijima, and T. Ishikawa, Sci. Rep. **5**, 18488 (2016).
[45] G. Vizsnyiczai, G. Frangipane, S. Bianchi, F. Saglimbeni, D. Dell'Arciprete, and R. Di Leonardo, Nat. Commun. **11**, 2340 (2020).